Efficient Broadband Electromagnetic Modeling of Anechoic Chambers

Zubiao Xiong[1], Zhong Chen[1], Ji Chen[2]
[1]ETS-Lindgren, Cedar Park, TX, USA, zhong.chen@ets-lindgren.com
[2]Department of Electrical & Computer Engineering, University of Houston, Houston, TX, USA, jchen18@uh.edu

***Abstract*—An efficient method is presented to numerically model anechoic chambers ranging from VHF to microwave frequencies. In this method, an approximate image theory is proposed to improve the accuracy of plane wave assumptions used at lower frequencies. At high frequencies, an efficient image-based ray tracing algorithm is developed which integrates with the approximate image theory seamlessly. Numerical results demonstrate the applications in the analysis of anechoic chambers for both low frequency and high frequency ranges.**

***Index Terms*— Anechoic chamber, electromagnetic propagation, approximate image thoery, ray tracing.**

I. INTRODUCTION

Numerical analysis of anechoic chambers is an important topic in the area of electromagnetic measurements nowadays. A variety of numerical methods can be used for computing the electromagnetic field inside an anechoic chamber. Full wave solvers, such as finite element method (FEM), finite difference in time domain (FDTD), method of moments (MoM), and multi-level fast multipole method (MLFMM), can accurately solve Maxwell's equations [1]. However, we are faced with a very large number of unknown variables due to the large electrical size of the chamber and the complicated structure of absorbing materials. Even with state-of-the-art computers, the large memory and time requirements may render them impractical, especially for higher frequencies. Therefore, high-frequency approximation techniques, such as ray tracing method, became attractive and extensively employed in the industry due to their high efficiency. However, the high-frequency approximation assumes plane wave conditions at the chamber surfaces. This assumption can potentially introduce large errors if the chamber walls are in the near zone of the transmitting and/or receiving antennas. Therefore, high frequency methods suffer from poor accuracy at lower frequencies. The lack of an efficient broadband solver has always been a main obstacle to the computer-aided design and optimization of anechoic chambers.

We developed an efficient method to model the anechoic chamber for a wide frequency range from tens of MHz to GHz. The method will be presented in this paper as follows. Section II.A briefly introduces the approximate image idea, which improves the low frequency accuracy of the ray tracing method. Section II.B presents an image-based ray tracing algorithm which is integrated with the approximate image theory seamlessly. Numerical examples for NSA (low frequency) and free space VSWR (high frequency) analysis of anechoic chambers are shown in section III. Section IV gives the conclusions.

II. METHODOLOGY

A. Approximate Images

In ray tracing methods used for electromagnetic analysis of anechoic chambers, an essential part is to model the electromagnetic field correctly for ray reflection. Considering the polarization of electromagnetic waves, a general approach to account for the ray reflection is [2, 3]

$$\bar{E}^r = \bar{\bar{\Gamma}}\bar{E}^i = \begin{bmatrix} \Gamma_{||} & 0 \\ 0 & \Gamma_{\perp} \end{bmatrix} \begin{bmatrix} E^i_{||} \\ E^i_{\perp} \end{bmatrix} \tag{1}$$

where the reflection coefficient dyad $\bar{\bar{\Gamma}}$ relates the incident electric field $\bar{E}^i$ and the reflected electric field $\bar{E}^r$. The subscripts $||$ and $\perp$ represent the components parallel and perpendicular to the plane of incidence (the plane which contains the normal vector of the reflection surface and the propagation vector of incidence), respectively.

This parallel/perpendicular decomposition approach assumes plane waves. For lower frequencies, this assumption may not be strictly valid, since the source may not be far away enough from the reflection surface. Instead of decomposing the electric fields into parallel and perpendicular components, we proposed to use approximate images of sources [4]:

$$\bar{J}^{IM} \approx \Gamma_{\perp} J^s_{\perp} \hat{e}_{\perp} - \Gamma_{||} J^s_{\rightarrow} \hat{e}_{\rightarrow} + \Gamma_{||} J^s_{\uparrow} \hat{e}_{\uparrow} \tag{2}$$

$$\bar{M}^{IM} \approx \Gamma_{||} M^s_{\perp} \hat{e}_{\perp} - \Gamma_{\perp} M^s_{\rightarrow} \hat{e}_{\rightarrow} + \Gamma_{\perp} M^s_{\uparrow} \hat{e}_{\uparrow} \tag{3}$$

where $\bar{J}^s = \left[J^s_{\perp}, J^s_{\rightarrow}, J^s_{\uparrow}\right]^T$ is the electric current density source, and $\bar{M}^s = \left[M^s_{\perp}, M^s_{\rightarrow}, M^s_{\uparrow}\right]^T$ is the magnetic current density source. The subscripts $\perp$, $\uparrow$, and $\rightarrow$ represent the component perpendicular to the plane of incidence, the component perpendicular to the reflection surface, and the component orthogonal to the other two components. $\hat{e}_{\perp}$, $\hat{e}_{\rightarrow}$,

978-88-907018-7-0/17/$31.00 ©2017 IEEE

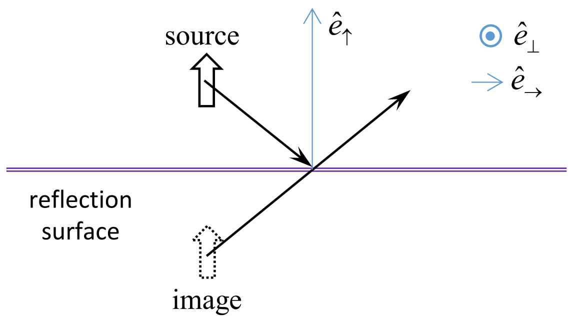

Fig. 1. Illustration of ray reflection at the medium interface.

and $\hat{e}_\uparrow$ are unit vectors along three orthogonal directions, as shown in Fig. 1. The approximate images $\overline{J}^{IM}$ and $\overline{M}^{IM}$ locate at the positions of the corresponding mirror images.

The reflected electric field can then be calculated as

$$\begin{aligned}\overline{E}^r(\overline{r}) = &-j\omega\mu_0 \int \overline{\overline{G}}(\overline{r}-\overline{r}')\cdot \overline{J}^{IM}(\overline{r},\overline{r}')d\overline{r}' \\ &+ \int \overline{M}^{IM}(\overline{r},\overline{r}')\times \nabla g(\overline{r}-\overline{r}')d\overline{r}'\end{aligned} \tag{4}$$

where

$$\begin{aligned}g(\overline{R}) &= \frac{e^{-jk_0|\hat{R}|}}{4\pi|\hat{R}|} \\ \overline{\overline{G}}(\overline{R}) &= \left(\overline{\overline{I}} + \frac{\nabla\nabla}{k_0^2}\right)g(\overline{R})\end{aligned} \tag{5}$$

where ω is the angular frequency, μ_0 is the permeability in vacuum, k_0 is the wave number in vacuum, and $\overline{\overline{I}}$ is the unit dyadic.

If the sources move far away from the reflection surface, (4) asymptotically approaches (1). Thus, the proposed approximate image method converges to the parallel/perpendicular field decomposition method for the far-field case. The major benefit of the approximate image method is that it is much more accurate for near-field cases. Let us consider the reflection on a perfect electric conductor (PEC) or a perfect magnetic conductor (PMC) surface. It is easy to find that (2) and (3) reduce to the well-known image theory in these cases, which can be used at any distance and any frequency. In other words, the proposed approximate image method is exact for PEC/PMC. For general absorbing materials, it is only asymptotically exact when the distance approaches infinity. But its accuracy is surprisingly acceptable in many near-zone cases according to our experiences [4]. Compared against the parallel/perpendicular field decomposition method, approximate image method preserves the field components along the direction of propagation, which have been neglected by the far field image theory. The approximate image method addresses a major error source for low frequency chamber modeling.

B. *Image-based ray tracing*

Since the approximate image locate at the exact same position as the mirror image, we could naturally use the geometric optics (GO) to find the images for multiple orders of reflections. After each reflection, the corresponding approximate images are treated as a new source for the next reflection. We keep finding the approximate images recursively until the order of reflection meets a preset criterion. Eventually, we locate a set of approximate images. It is worth noting that, only the locations, not the values, of the approximate images are determined initially. The values of the approximate images may only be assigned after the actual ray path from the original transmitting source (Tx) to the receiving point (Rx) is established, since they depend on the incident-angle-dependent reflection coefficients. Once the values are determined, we can calculate the reflected fields at the receiving point according to (4).

Specifically, considering that we might want to obtain the field at multiple receiving points for multiple frequencies, we follow these steps to eliminate redundant calculations:

1) Building the visibility tree: The root of the visibility tree is the transmit antenna (Tx). The first level consists of all flat reflecting surfaces of the anechoic chamber which can be illuminated by the Tx. Each node in the first level includes a reflecting surface and its corresponding mirror image of the Tx. The mirror image is the new source to the next level, whose field of view is limited by the reflecting surface. Thus, this mirror image illuminates only a part of the chamber through the "window" defined by the reflecting surface. The illuminated part of the chamber is then decomposed into multiple flat surfaces, filling into the next level of the visibility tree. We then find the mirror images of the parent's image, and make the child images illuminate instead. We do it recursively for each node in the first level, and build up the whole visibility tree. This step only needs the information of the Tx and the geometric reprenstation of the anechoic chamber. The same visibility tree is applicable for all succeeding steps.

2) Finding all ray paths from Tx to each Rx: For each receive antenna (Rx) position, we could now find all possible ray paths from the Tx. We start searching from the terminal nodes of the visibility tree by checking if the Rx is illuminated by the node's image source. If it is illumated, there is a valid ray path traveling from the root (Tx) to the node. The last reflection point of this ray path is just the intersection point between the node's reflecting surface and a straight line which connects the Rx and the node's image. We then connect the last reflection point with the image of the parent node, and trace all the way back to the root by following the same procedure. All these reflection points make up the ray path. The only additional knowledge required by this step is the positions of each Rx. The calculation so far has been independent of frequency. The generated ray path data are reusable for the following frequency-dependent calculations.

3) Determining the approximate image value for each ray path at each Rx position for each frequency: We need to determine the value of the last approximate image of each ray path for field calculation. This value can be obtained by tracing all levels of images along the ray path and applying (2) or (3) one at a time. The field calculated from the last approximate image is the final reflected field exiting from the ray path.

4) Calculaing the electric field at each Rx for each frequency: This step is straightforward. Summing up the contributions from all approximate images and the direct Tx incident field yields the total electric field.

III. NUMERICAL RESULTS

A. NSA analysis (low frequency)

Normalized site attenuation (NSA) is an important metric that is used to define the performance of a semi-anechoic chamber (which is widely used in EMC testing). According to standard CISPR 16-1-4 [5] and ANSI C63.4 [6], the measured NSA for a semi-anechoic chamber must be within ±4 dB of the theoretical NSA. The theoretical NSA can be found from the tabular data in [6], or calculated according the formulas presented in [7]. The NSA prediction can be derived as follows:

$$NSA = \frac{|V_I|}{\max|V_R| \cdot AF_T \cdot AF_R} \tag{6}$$

where V_I is the voltage fed into the Tx, V_R is the received voltage of the Rx in the simulation, and AF_T and AF_R are the antenna factor of Tx and Rx respectively. Rx scans in a certain range of various heights. Then the maximum magnitude of the Rx output in the height-scan range is used for calculating the predicated NSA.

A chamber of size 22.6 m × 13.6 m × 8.7 m is used for NSA analysis validation. The distance between Tx and Rx is 10 m. The height of Tx is fixed at 2 m for horizontal polarization and 1.5 m for vertical polarization. Rx scans from 1 to 4 m height. Complex absorber reflectivity for both parallel and perpendicular polarizations as a function of incident angle and frequency is computed by HFSS, and is used subsequently in the ray tracing simulation. Fig. 2 shows the comparison between the simulated NSA and the ideal NSA for two polarizations. As can be seen, the simulation results fall within ±4 dB range of the ideal values. The comparison against measurement data will be conducted in the next stage.

B. Free space VSWR analysis (high frequency)

Free-space VSWR method is widely used for evaluating fully lined anechoic chambers in a microwave chamber. In the free-space VSWR method, we obtain the reflectivity by measuring the amplitude ripple at a given frequency (standing wave) across a line in the quiet zone. The chamber reflectivity is defined as [8, 9]

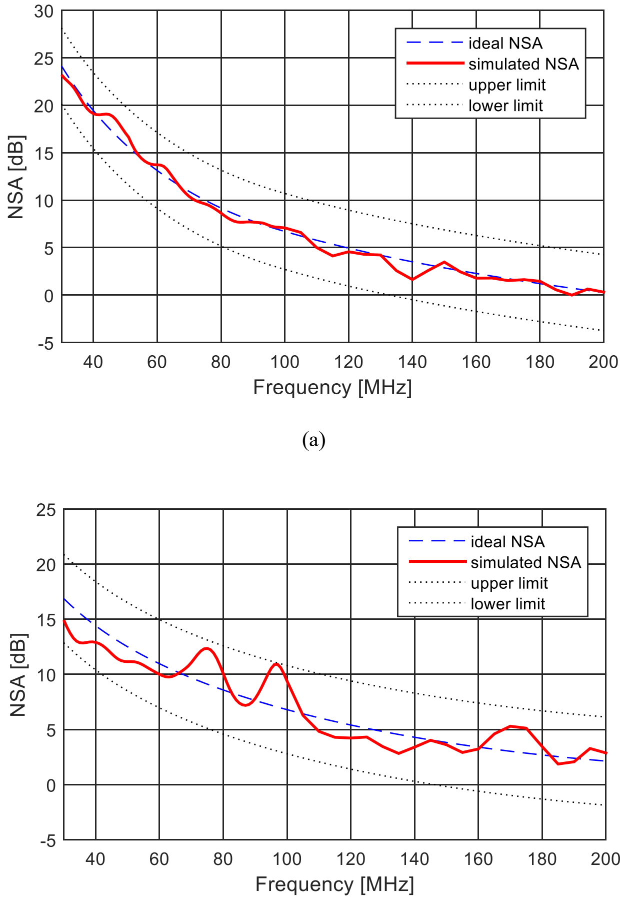

Fig. 2. Comparing the NSA prediction of the proposed method against the ideal NSA with the polarization: (a) horizontal; (b) vertical.

$$R = P(\alpha)\frac{VSWR-1}{VSWR+1} \tag{7}$$

$$VSWR = \frac{E_d + \sum E_r}{E_d - \sum E_r} \tag{8}$$

where E_d and E_r are the direct incident electric field coming from the Tx and the reflected electric field coming from the chamber into the quiet zone (QZ), respectively. $P(\alpha)$ is the probe (receive) antenna pattern.

A 20’ (l) x 10’ (w) x 8’ (h) chamber is simulated using ray tracing method. The antennas are separated by 15’. The simulation is performed at 6 GHz. After a ray hits the

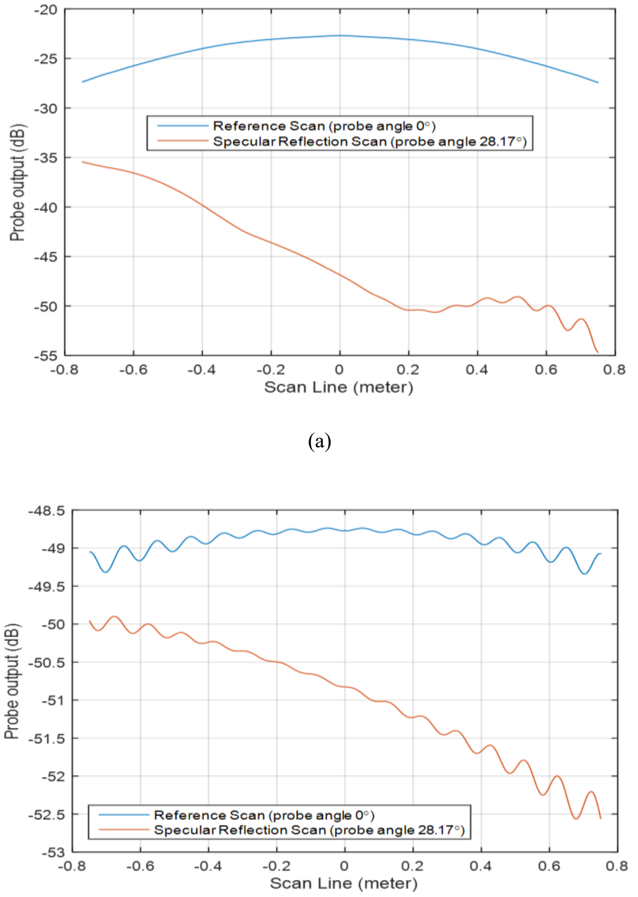

(a)

(b)

Fig. 3. Probe output along scan line for: (a) high gain probe, R = -41.8 dB based on the chart; (b) low gain probe, R = -33.1 dB based on the chart.

absorber surface twice, the wave is considered negligible. The probe rotation angle is set at 28 degrees, pointing at the specular point on the side wall. The probe travels transversely along a 1.5 m distance. Two probe antennas are considered, one is a high gain antenna with a peak gain of 19.1 dBi, and another is a low gain antenna with a peak gain of 6.2 dBi. Fig. 3 shows the simulation scan results. Applying (7), the chamber reflectivity is calculated to be -41.8 dB when using the high gain probe, and -33.1 dB when using the low gain probe.

Fig. 4 shows the chamber reflectivity results as a function of probe angle. The simulation results showed that the chamber reflectivity is dependent on the gain of the probe.

IV. CONCLUSIONS

We presented an approximate image based ray tracing method for modeling anechoic chambers in a wide frequency range. The approximate image theory we proposed is much more accurate than the traditional parallel/perpendicular field decomposition technique when near-field effect is not negligible. Therefore, the proposed method has the ability to model anechoic chambers at low frequencies (e.g., VHF range), meanwhile, retaining the efficiency of the ray tracing technique.

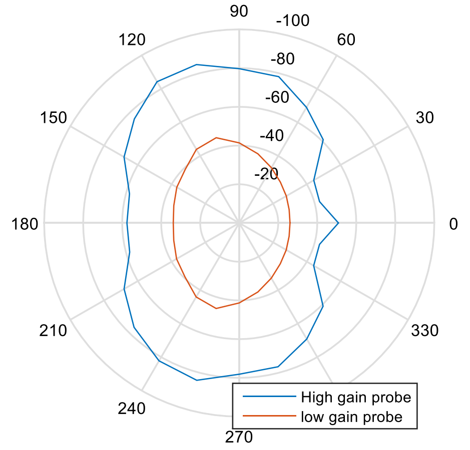

Fig. 4. Chamber reflectivity for all angles (vertical polarization/transverse scan).

Numerical examples including NSA prediction and free-space VSWR reflectivity analysis were conducted to demonstrate the versatility of the proposed method. This method can also be applied to many other applications such as RCS computation of dielectric objects, and indoor wave propagation modeling. More validations and applications will be performed in the future.

REFERENCES

[1] D. Campbell, G. Gampala, and C. Reddy, “Modeling and Analysis of Anechoic Chamber Using CEM Tools,” Appl. Comput. Electromagn. Soc. J., vol. 28, no. 9, pp. 755–763, 2013.

[2] H. Ling, R.-C. Chou, and S.-W. Lee, “Shooting and bouncing rays: Calculating the RCS of an arbitrarily shaped cavity,” IEEE Trans. Antennas Propag., vol. 37, no. 2, pp. 194–205, 1989.

[3] Q. Xu, Y. Huang, X. Zhu, L. Xing, P. Duxbury, and J. Noonan, “Building a better anechoic chamber: a geometric optics-based systematic solution, simulated and verified,” IEEE Antennas Propag. Mag., vol. 58, no. 2, pp. 94–119, 2016.

[4] Z. Xiong, J. Chen, and Z. Chen, “Low frequency modeling for electromagnetic analysis of arbitrary anechoic chambers,” in IEEE International Symposium on Electromagnetic Compatibility, 2016, in press.

[5] CISPR 16-1-4, Specification for radio disturbance and immunity measuring apparatus and methods - Ancillary equipment - Radiated disturbance, 2007.

[6] ANSI, American National Standard for Methods of Measurement of Radio Noise Emission from Low Voltage Electrical Equipment in the Range 9 kHz to 40 GHz, ANSI Std. C63.4, 2001.

[7] A. A. Smith, R. F. German, and J. B. Pate, “Calculation of Site Attenuation from Antenna Factors,” IEEE Trans. Electromagn. Compat., vol. EMC-24, no. 3, pp. 301–316, 1982.

[8] Z. Chen, Z. Xiong, and A. Enayati, “Limitations of the free space VSWR measurements for chamber validations,” in 38th Annual Meeting and Symposium of the Antenna Measurement Techniques Association, 2016, unpublished.

[9] University of Michigan Report 5391-1-F, February 1963 (Free space VSWR test).